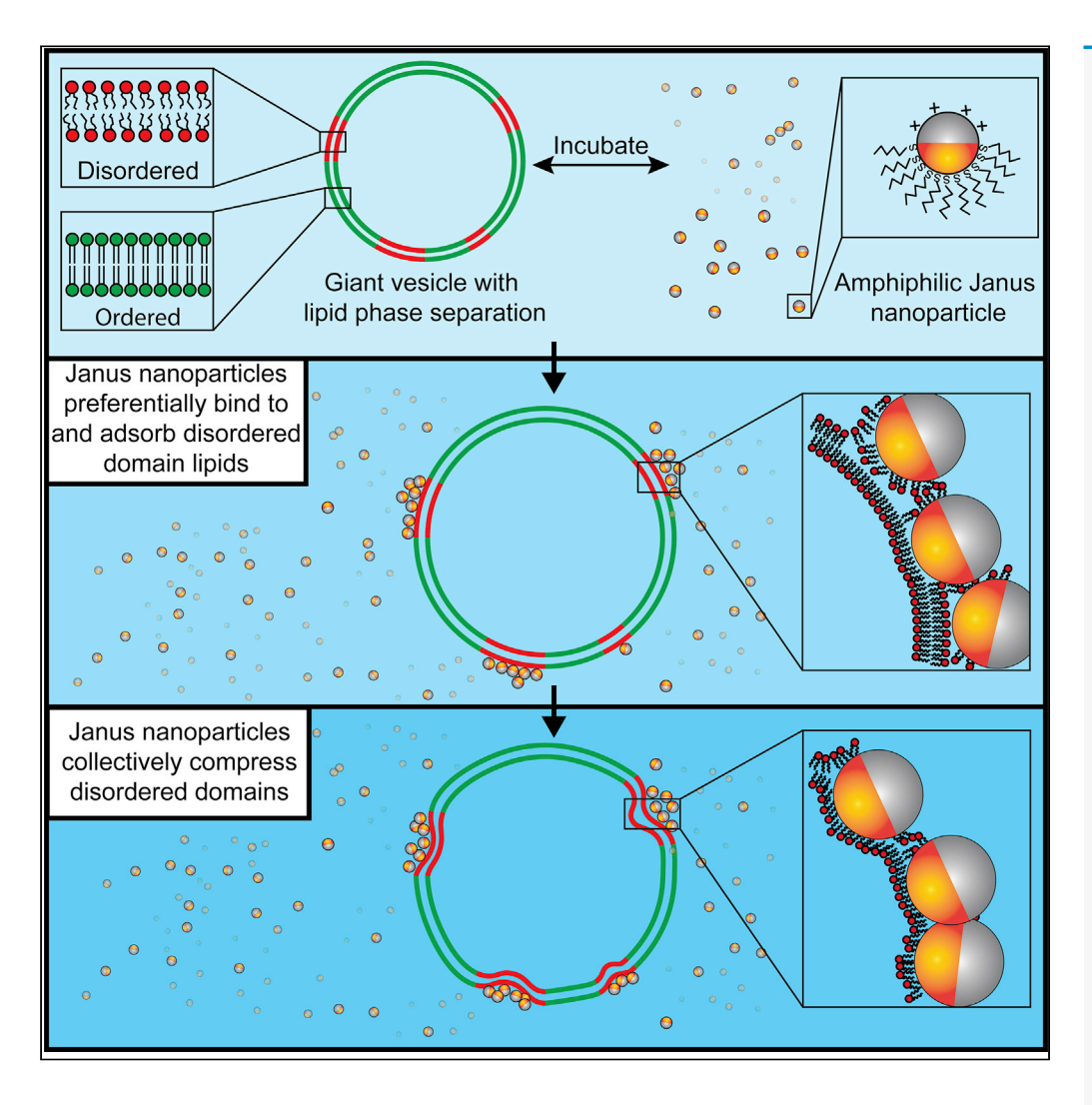
iScience



Article

Domain-selective disruption and compression of phase-separated lipid vesicles by amphiphilic Janus nanoparticles



Jared T. Wiemann, Danh Nguyen, Ying Li, Yan Yu

ying.3.li@uconn.edu (Y.L.) yy33@indiana.edu (Y.Y.)

Highlights

Amphiphilic Janus nanoparticles (NPs) deform phase-separated lipid vesicles

Janus NPs preferentially extract lipids from liquiddisordered membrane domains

Tension from lipid loss and inter-particle attractions compress vesicle membranes

Wiemann et al., iScience 25, 105525 December 22, 2022 © 2022 The Author(s). https://doi.org/10.1016/ j.isci.2022.105525



iScience



Article

Domain-selective disruption and compression of phase-separated lipid vesicles by amphiphilic Janus nanoparticles

Jared T. Wiemann, 1,4 Danh Nguyen, 2,3,4 Ying Li, 2,3,* and Yan Yu^{1,5,*}

SUMMARY

Janus nanoparticles (NPs) with anisotropic surface functionalities enable unique biomedical applications, but their interaction with the biomembranes cannot be predicted by models derived from nanoparticles with uniform surface chemistry. Here, we combine experiments with molecular dynamics (MD) simulations to investigate the interaction of amphiphilic Janus NPs, which are cationic and hydrophobic on opposite sides, with lipid vesicles exhibiting phase-separated microdomains. We demonstrate that Janus NPs preferentially bind to and extract lipids from liquid-disordered domains over a broad range of vesicle compositions. This domain-selective membrane disruption and the inter-particle attractions concurrently generate a compression force on the vesicle, causing the remaining liquid-ordered domains to bulge and the entire vesicle to wrinkle. The NP-induced membrane compression and deformation are critically driven by the surface anisotropy of the Janus NPs. The findings highlight the feasibility of using the surface anisotropy of NPs to tailor their interactions with different biological membranes.

INTRODUCTION

Janus nanoparticles (NPs), particles that have two distinct surface makeups or compartments, enable biomedical applications inaccessible to uniform nanoparticles. ^{1–5} For example, the two-faced architecture spatially separates functions that would otherwise interfere when mixed, such as cell targeting and molecular sensing, so that incompatible capacities can be combined into a single unit of structure. ^{6,7} To realize these promising applications, Janus particles must successfully cross the cell membrane to function inside cells. Yet little is known about how the surface anisotropy of these particles influences their interaction with the cell membrane, which is the first barrier to their cellular entry. For NPs with a uniform composition or surface chemistry, extensive studies have revealed how their physiochemical properties, such as size, shape, and surface charge, affect the integrity and function of biological membranes, ^{8–16} but these findings are insufficient to predict the biological impact of Janus NPs with anisotropic surface coatings. Computer simulations have suggested that interactions between Janus NPs and bio-membranes lead to unique phenomena, such as membrane insertion ^{17–19} and pore formation. ^{20,21} But the simplifications used in simulation models limit their usefulness as guides to complex experimentally relevant systems. Therefore, new experimental knowledge of Janus particle-membrane interactions is critically needed to harness the promising potential of Janus particles in biomedical applications.

In recent years, our group has systematically evaluated how the anisotropic surface chemistry of Janus NPs affects their interactions with lipid membranes. We first reported that amphiphilic Janus NPs that are hydrophobic and cationic on opposite hemispheres induce pores in planar lipid bilayers composed of zwitterionic lipids. Janus NPs extract lipids onto their hydrophobic hemispheres, which increases membrane tension that eventually leads to membrane rupture. We further showed that when multiple amphiphilic Janus NPs simultaneously interact with a single giant unilamellar vesicles (GUVs), they collectively exert a compression force on the vesicle's membrane, leading to "wrinkling" membrane deformation and even vesicle rupture. Those findings imply an interesting model that Janus NPs of sizes significantly larger than the thickness of a lipid bilayer, disrupt lipid membranes by compression instead of by translocation. The Janus NP-induced membrane compression was attributed to an interplay between particle-membrane interaction and inter-particle attraction driven by particle hydrophobicity. Interestingly, some recent

2022.105525



¹Department of Chemistry, Indiana University, Bloomington, IN 47405, USA

²Department of Mechanical Engineering and Polymer Program, Institute of Materials Science, University of Connecticut, Storrs, CT

³Department of Mechanical Engineering, University of Wisconsin-Madison, Madison, WI 53706, USA

⁴These authors contributed equally

⁵Lead contact

^{*}Correspondence: ying.3.li@uconn.edu (Y.L.), yy33@indiana.edu (Y.Y.) https://doi.org/10.1016/j.isci.





studies suggest that NPs with uniform surface coatings, with sufficiently strong inter-particle attraction, may also induce a compression effect on the outer membrane of bacteria. ^{26,27} This model of NP-induced membrane compression opened doors to many exciting scientific questions. One particularly important one is: how does such compression effect influence lipid membranes with phase-separated microdomains, which is an indispensable feature of the plasma membrane of living cells?

Here, we address this question by combining quantitative imaging experiments with coarse-grained molecular dynamics (MD) simulations. Our experimental platform is GUVs composed of 1,2-dioleoyl-sn-glycero-3-phosphocholine (DOPC), 1,2-dipalmityl-sn-glycero-3-phosphocholine (DPPC), and cholesterol (Chol). These lipids have different liquid-to-gel transition temperatures. Over a broad range of lipid composition and temperature, the mixture of DOPC, DPPC, and cholesterol phase separate into coexisting liquid phases that appear as micron-sized membrane domains. The liquid-disordered (Ld) microdomains are rich in the unsaturated DOPC lipid, whereas the liquid-ordered (Lo) microdomains are rich in the saturated DPPC lipid. We investigated, over a broad range of lipid membrane compositions, how amphiphilic cationic/hydrophobic Janus NPs interact with the different membrane domains. We found that Janus NPs preferably bind to and extract lipids from the DOPC-rich Ld domains on GUVs. This causes not only the disappearance of Ld domains but also the bulging of Lo domains that remain in the GUV membrane. Using coarse-grained MD simulations, we revealed the time-dependent evolvement of the composition of lipids extracted by Janus NPs and the compression of the GUV membranes at various compositions.

RESULTS AND DISCUSSION

Janus nanoparticles preferentially bind to liquid-disordered domains

GUVs used in this study consisted of DOPC, DPPC, and cholesterol (Chol). They were formed in 100 mM sucrose solution under alternating electrical field.²⁹ This mixture of lipids is known to phase separate into DOPC-enriched Ld and DPPC-enriched Lo membrane domains at room temperature over a broad range of lipid compositions.³⁰ To visualize the different membrane domains using fluorescence microscopy, we added in the lipid mixture RhB-DOPE (0.2 mol%) and BODIPY-Chol (0.2 mol%), which selectively partition into the Ld and Lo phases, respectively (Figure S1). 31,32 We added 40 pM Janus NPs (100 nm in diameter) to GUVs of four different lipid compositions, 1:3:1 (DOPC:DPPC:Chol), 1:1:1, 2:2:1, and 1:2:2, and after 30 min examined the membrane morphology using confocal fluorescence microscopy (Figures 1A-1E). These different lipid ratios cover a broad range of the Lo-Ld phase coexistence region of the DOPC-DPPC-Chol phase diagram³⁰ and are therefore suitable for testing the generality of our observations. We made two observations. First, for all four lipid compositions, Janus NPs preferentially adsorbed on the Ld membrane domains and induced deformation of those membrane domains. Second, the Janus NPs, which appeared as dark dots in brightfield and fluorescence images due to their partial metal coatings, formed aggregates near the Ld domains (marked by RhB-DOPE fluorescence). The Janus NP aggregates colocalized with puncta of strong RhB-DOPE fluorescence. This was later confirmed to be Janus NPs wrapped with lipids from the Ld domains.

To quantify the first observation of preferential binding of Janus NPs to Ld membrane domains, we measured particle binding kinetics to the Lo and Ld membrane domains. We prepared phase-separated planar lipid bilayers on glass coverslips by rupturing phase-separated GUVs with the 2:2:1 lipid composition ratio. 33 The exact composition of the Ld and Lo domains can vary slightly at different overall membrane compositions, but this does not affect the preferential binding of Janus NPs to the Ld domains, which was observed for all four lipid compositions examined (Figures 1A-1E). Therefore, the Janus NP-membrane binding result from the 2:2:1 membrane composition is expected to be representative of that of the other three compositions. As in GUV membranes, the Ld and Lo membrane domains were labeled with RhB-DOPE and BODIPY-Chol, respectively (Figure 1F). We then fluorescently labeled the Janus NPs with a small amount of Cy5 dyes (particle characterization in Figure S2). Using total internal reflectance fluorescence (TIRF) microscopy, which illuminates only about 100-200 nm depth above the glass substrate, we imaged only Janus NPs adsorbed on the membranes instead of those freely diffusive in the solution. After counting the surface density of Janus NPs adsorbed on the Lo and Ld domains, separately, as a function of time (Figure 1G), we calculated the Janus NP-membrane binding rate constant (k_a) by assuming a second-order particle-membrane binding process (Figure 1H).^{23,34} We found that Janus NPs bind to the Ld membrane phase with a $k_a = 66,000 \pm 6,000 \, \mathrm{M}^{-1} \, \mathrm{s}^{-1}$, larger than the k_a for their binding to the Lo phase $(k_a = 52,000 \pm 6,000 \text{ M}^{-1} \text{ s}^{-1})$. The activation energies for Janus NP binding to the Ld and Lo phases were 40.8 \pm 0.2 kJ/mol and 41.4 \pm 0.3 kJ/mol, respectively (see detail of calculation in Experimental



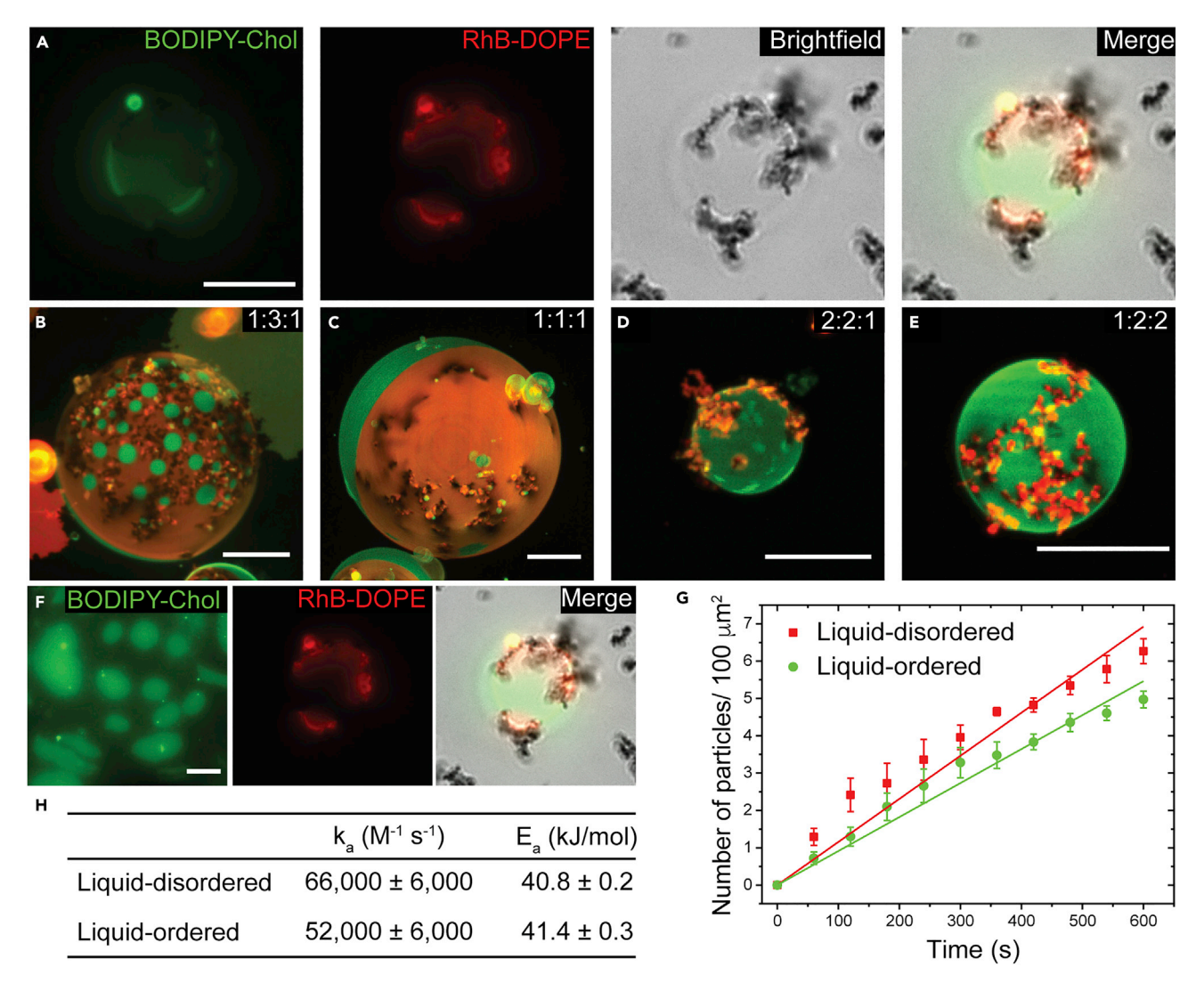


Figure 1. Janus NPs preferentially bind to Ld domains

(A) Epi-fluorescence images of a 1:3:1 (DOPC: DPPC:Chol) GUV after interacting with 40 pM Janus NPs for 30 min. Liquid-disordered (Ld) domains (marked by RhB-DOPE) are shown in red, and liquid ordered (Lo) domains (marked by BODIPY-Chol) are shown in green. Brightfield image shows Janus NPs on the GUV.

(B–E) Z-projection confocal fluorescence images of GUVs of 1:3:1 (B), 1:1:1 (C), 2:2:1 (D), and 1:2:2 (E) compositions after 30-min interaction with 40 pM Janus NPs

(F) Epi-fluorescence images showing a phase-separated planar lipid bilayer (2:2:1 composition) made from GUV rupture. Lo and Ld domains are presented in green and red, respectively.

(G) Plots showing surface densities of Janus NPs (number of NPs per $100~\mu m^2$) adsorbed on Ld and Lo domains as a function of time. Data are represented as mean \pm SEM from three independent samples.

(H) Binding rate constant (k_a) and activation energy (E_a) calculated from plots in (G). Scale bars: 10 μ m. See also Figures S1 and S2.

section). These results quantitatively confirm that Janus NPs preferentially bind to the Ld membrane domains. However, the difference in k_a is surprisingly smaller than expected based on our observation that the Janus NPs almost exclusively adsorbed on the Ld domains of GUVs (Figures 1A–1E). This might be because free-standing vesicle membranes and glass-supported planar membranes, which were used for binding kinetics measurements, have different bending rigidities and undulation, which are known to affect the adsorption of particles. The addition, the frictional coupling between lipids and the underlying glass substrate can lead to reduced membrane fluidity and hinders the Ld-Lo phase separation in membranes. The additional results are intrinsically more stiff and less fluidic than the Ld domains, the glass substrate likely impacts the Ld domains more and therefore reduces the differences in the lipid



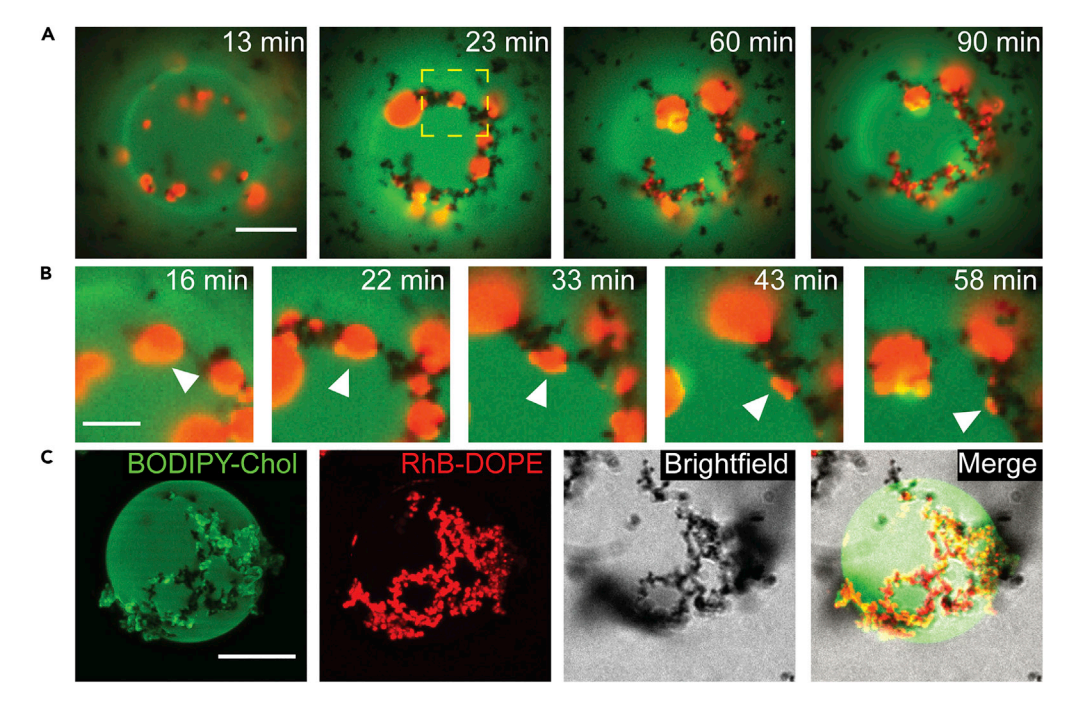


Figure 2. Janus NPs preferentially disrupt Ld domains in GUVs

(A) Time-lapse epi-fluorescence images showing interactions of Janus NPs with the Ld domains (shown in red) on a GUV of 1:2:2 composition.

(B) Zoomed-in time-lapse images from the area outlined in (A). White arrows indicate a Ld domain that shrank during interaction with Janus NPs.

(C) Fluorescence z-projections and brightfield image of a representative 1:2:2 GUV in the presence of 40 pM Janus NPs. Scale bars: 10 μ m in (A) and (C); 5 μ m in (B). See also Figures S3–S6; Videos S1 and S2.

packing structure between the Ld and Lo domains. As a result, the selective binding of Janus NPs to the Ld domains becomes less prominent on the glass-supported bilayers compared to that on the free standing giant vesicle membrane.

We next sought to understand the observation of Janus NP aggregates that colocalized with puncta of strong RhB-DOPE fluorescence (marker for Ld domains) (Figures 1A–1E). To test whether those puncta are curved membrane domains or lipids wrapping around Janus NPs, we increased the temperature of the GUV solutions to as high as 45°C. The idea is that if those puncta are membrane domains, they would disappear at the temperature higher than the phase mixing temperature. The mixing temperature of the 1:2:2 GUVs is reportedly $\sim 35-37^{\circ}$ C. Indeed, we observed that the Ld and Lo domains of the 1:2:2 GUVs, without Janus NP interactions, became completely mixed when the temperature was raised to 40°C (Figure S3, N = 70 out of 70 GUVs). In contrast, the membrane puncta that were formed after interaction with Janus NPs remained unchanged at temperatures as high as 45°C (Figure S4, N = 10 out of 10 GUVs). This indicates that the membrane puncta of strong RhB-DOPE fluorescence are lipids that formed complexes with Janus NPs.

To gain more insights into how Janus NPs interact with the Ld domains, we performed real-time imaging of 1:2:2 GUVs interacting with 40 pM Janus NPs using fluorescence confocal microscopy. The Janus NPs appeared as dark spots in the time-lapse fluorescence images because their gold caps blocked light. A representative GUV is shown in Figure 2A and Video S1, which were acquired about 12–13 min after Janus NPs were added to GUVs. At first, the Ld domains in the GUV membrane were well dispersed. Janus NPs bound to different Ld domains without forming any large aggregations. Gradually, the Ld domains together with the bound Janus NPs moved toward one another on the GUV membrane and also generally toward the bottom of the GUV, until the Janus NPs formed large chain-like aggregations. It is possible that the Ld domains were brought into proximity by the coalescence of Janus NPs and they moved to the bottom of the GUV due to the weight of Janus NP aggregates that were bound. During this process, many Ld domains began to shrink while the bound Janus NPs became more fluorescent (Figure 2B). This indicates that lipids



were extracted, mostly from the Ld domains, and transferred onto Janus NPs. For some GUVs, Ld domains disappeared completely, leaving only Lo domains and the lipid-Janus NP complexes (Figure 2C and Video S2). This Janus NP-induced reorganization and shrinking of Ld membrane domains was observed in about 40% of all 1:2:2 GUVs (more examples in Figure S5) and in GUVs of other membrane compositions to a lesser extent (Figure S6). We postulate that this is because the 1:2:2 composition, among all compositions studied here, had the lowest fraction of DOPC and thus the smallest surface area of Ld domains. In this case, the Janus NPs have a sufficient surface area to extract most, or all, lipids from the Ld domains, resulting in the shrinking and disappearance of many Ld domains. This speculation was later confirmed by our coarse-grained MD simulations.

These real-time imaging data indicate that Janus NPs interact with the phase-separated membranes in three steps: (1) Janus NPs bind preferentially to Ld domains, (2) form aggregates themselves and induce the aggregation of attached Ld domains, and (3) extract lipids from Ld domains. The chain-like aggregation of Janus NPs is likely formed due to a delicate interplay between particle-membrane binding energy and bending rigidity of the membrane, similar to what was reported in a previous simulation study.³⁹

Molecular dynamics simulation of Janus nanoparticle-planar membrane interactions

We next performed coarse-grained MD simulations using a modified version of the MARTINI force filed⁴⁰ to further understand the binding interaction between Janus NPs and phase-separated membranes at the molecular scale. Due to the different length scales between experiments (micronscale) and MD simulations (nanoscale), the size of our computational models must be optimized to balance computational accuracy and efficiency. First, the size of the Au core was chosen to be 10 nm. This particle size is larger than the thickness of the lipid bilayer, which is similar to experiments. With this simulation particle size, we can observe the Janus NP-membrane interaction while maintaining reasonable computational cost. If the size of the Janus NP's core were the same as in experiments (100 nm), the computational model will be exceedingly large. Consequently, it will be too time-consuming to assess the time-dependent particle-membrane interactions. On the other hand, if the core of the particle is too small, the particle might embed into the lipid bilayers, which makes us difficult to perceive the disruption effects of Janus NPs. Secondly, the lipid bilayers were chosen as a planar membrane that can be compared with experimental works because the size of GUVs used in the experiments is much larger than the size of real Janus NPs (Janus NP's diameter/ GUV's diameter \sim 1/100). Finally, the size of the planar bilayers was chosen as 30 \times 30 nm² to facilitate the obvious formation of microdomains⁴¹ with computational efficiency and afford the size of Janus NP without the effect of boundary conditions.

The coloring schematics of coarse-grained lipids and Janus NP are presented in Figure 3A. For phase-separated planar membranes, a modified version from standard MARTINI⁴⁰ was adapted to ensure the formation of Ld and Lo domains in the bilayer model (Figure S7). Because the ratio of 2:2:1 (DOPC:DPPC:Chol) was mainly used in the experiment as well as in measuring the binding energy to specific domains in Figure 1H, we decided to use this ratio for the simulation of selective binding of Janus NP. First, a 2:2:1 (DOPC:DPPC:Chol) lipid bilayer was assembled in the absence of Janus NPs. After being equilibrated for 15 μ s, these lipids spontaneously organized into a Ld domain (DOPC-rich, red) and a Lo domain (DPPC-rich, green). Specifically, the Ld domain contained 88.2% of DOPC and the Lo domain contained 64.8 and 32.9% of DPPC and Chol, respectively. The averaged order parameter of the membrane and area per lipid plateaued after 15 μ s, (Figure S8), indicating the membrane was fully equilibrated for the next simulation step.

To investigate the binding preference of the Janus NP to the membrane domains, one Janus NP (core diameter $D_{NP}=10$ nm) was placed above the lipid domain boundary with its hydrophobic hemisphere pointing toward the membrane (Figure 3B at 0 μ s, full-time series in Videos S3 and S4). After 0.04 μ s, the Janus NP quickly extracted lipids from the Ld domain onto its hydrophobic hemisphere and began to disturb the bilayer. As the simulation further proceeded to 0.10 μ s, the NP was fully inserted into the Ld phase, causing domain wrinkling (Figure 3B at 0.10 μ s), and its hydrophobic hemisphere was completely covered with extracted lipids (Figure 3C). At the end of the simulation (1.00 μ s), the Janus NP remained inserted in the Ld domain with a tilted orientation, similar to what was observed for the interaction of the Janus NP with pure DOPC membranes. We also simulated a single Janus NP with a DOPC-only membrane, where the particle was inserted into the membrane in less than 0.10 μ s (Video S5). In contrast, when a similar simulation was done with a Lo membrane (6:4 DPPC:Chol), the Janus NP was never inserted into the



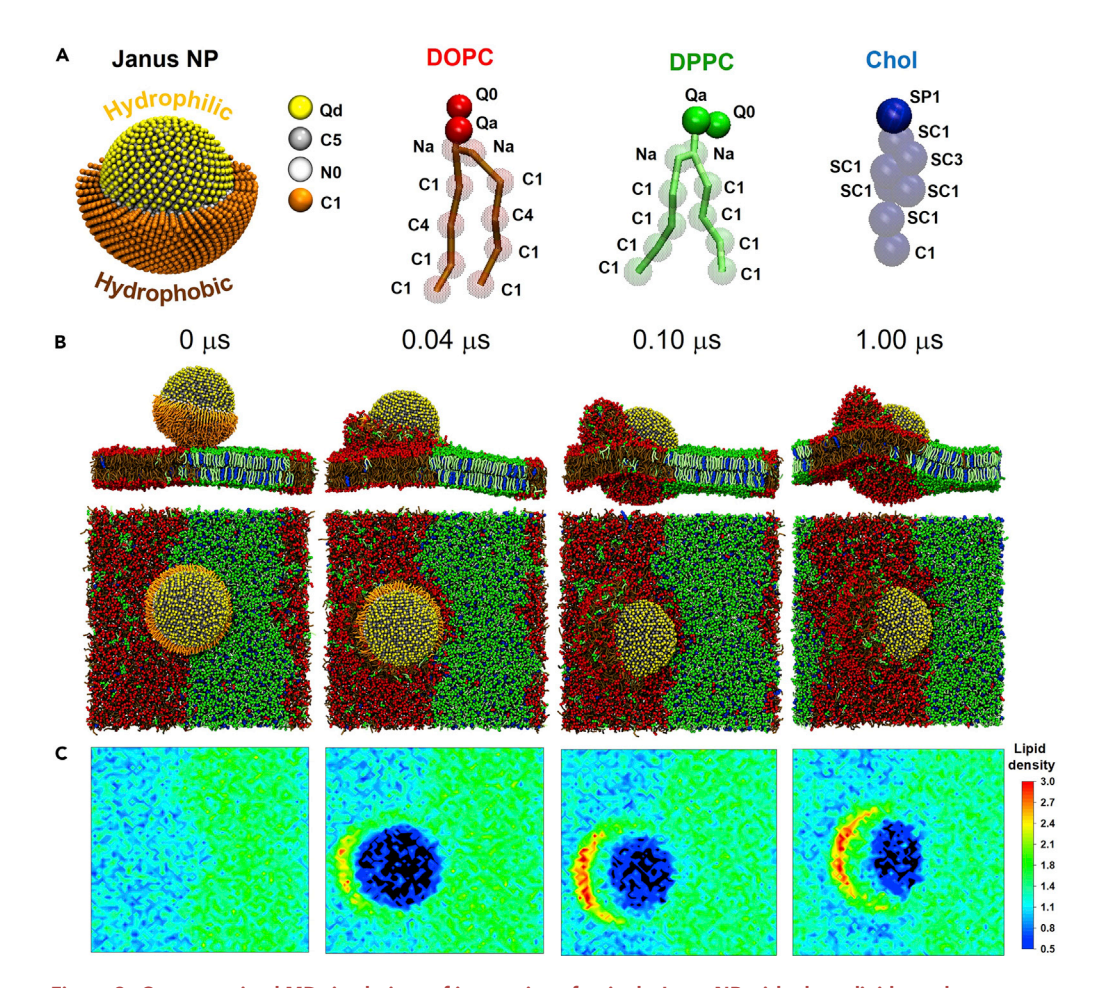


Figure 3. Coarse-grained MD simulations of interaction of a single Janus NP with planar lipid membranes
(A) Coarse-grained representations of Janus NP and lipids in MD simulations. Coloring scheme: Janus NP model contains
Au core (gray), sulfur (white), cationic ligand (yellow), and hydrophobic ligand (orange) beads; DOPC molecule contains
head group (red) and tails (brown) beads; DPPC molecule contains head group (green) and tails (lime) beads; Chol
molecule contains blue beads. The same coloring scheme is used for all MD simulations in this study.

(B) Representative snapshots (side and top views) showing the insertion of a Janus NP (core diameter $D_{NP}=10$ nm) into a phase-separated lipid bilayer (2:2:1 composition). Total simulation time is 1.00 μ s. Membrane dimension is \sim 30 \times 30 nm². Solvent molecules are included in simulation, but not shown here for clarity.

(C) Heatmaps of lipid density during Janus NP insertion into the phase-separated membrane corresponding to the MD snapshots in (B). See also Figures S7–S12; Videos S3, S4, S5, and S6.

membrane over the course of the simulation (Video S6). The different results further confirm the binding preference of Janus NPs to the DOPC-rich domain.

We then sought to understand the driving forces for the selective binding of Janus NPs to the Ld domains. Previous studies have shown that peptides of various types all preferentially partition into the Ld domains due to the lower lipid packing density in that domain compared to the Lo domain. 42,43 In our simulation, we first confirmed the lower lipid packing density of the Ld domains in our simulated membranes (Figure 3C). The packing density of DOPC lipids in the Ld domains changes significantly during interaction with Janus NPs, indicating the preferential interaction of NPs with the DOPC lipids (Figure S9). We also calculated the 2D landscape of order parameters (Figure S10) for the entire phase-separated lipid membrane. The order parameters of lipids (Scc) indicate the lipid ordering: the smaller the order parameter, the more disordered the lipids are. We found that the average order parameter of DOPC lipids in the membrane (Scc \sim 0.35) is less than half of that of DPPC lipids (Scc \sim 0.75). After interaction with Janus NPs, the average order parameter of DOPC also decreased more significantly (from Scc \sim 0.35 to \sim 0.2) than that of DPPC lipids (from Scc \sim 0.75 to \sim 0.7) (Figure S11). These results altogether suggest that Janus NPs preferentially interact with the



Ld domain because the lipids are more loosely packed compared to those in the Lo domain. The NP-induced disruption to the Ld domain causes lower energy costs than the disruption to the Lo domains (Figure S12). Specifically, we evaluated the binding free energy of the Janus NP toward different membrane domains by performing biased MD simulations through the umbrella sampling technique. ^{36,44} The potential mean force (PMF) measurements for these simulations were extracted as a function of the distance between the center-of-mass (COM) of the particle and the middle plane of a lipid bilayer. The PMF results of Janus NPs for the Ld and Lo domains revealed roughly an order of magnitude difference between Ld (~-120 kcal/mol) and Lo (~-12 kcal/mol) domains (Figure S12). This result demonstrates the substantial thermodynamic advantage of the Janus NP interaction with the Ld domain. For the Ld membrane, the system energy was dramatically minimized when the particle was inserted into the membrane (~5.6 nm COM distance) while for the Lo membrane, the system energy was minimized when the particle was resting on the membrane (~8.8 nm COM distance). Together, our results demonstrate that Janus NPs interaction with the Ld domain is thermodynamically favored compared to that with the Lo domain, because NP-induced disruption to the loose packing of the lipids in the Ld domain costs less energy.

We then investigated the collective effect of multiple Janus NPs on the phase-separated membrane by using four Janus NPs in the simulation. By doing so, we aim to simulate an extreme case of a very high local concentration of Janus NPs in a finite-size system, which is representative of the experimental condition where a high surface density of Janus NPs adsorbed on the GUVs membrane. We performed the MD simulation for 1.00 µs with the same parameter setup as for the single Janus NP simulation. We found that, while individual Janus NPs still inserted into the Ld domain and extracted lipids onto their hydrophobic hemisphere in a similar manner as for single Janus NP, their collective interactions caused the Ld domain to "wrinkle" (Figure 4A; Videos S7 and S8). As a result of this deformation, the x-y projection area of the planar membrane decreased significantly for all four compositions of membrane examined in terms of total planar area (Figure 4B) and domain (Ld/Lo) area (Figure S13). The calculation of the x-y projection area reduction is demonstrated in (Figure S14). Compared to single Janus NP, multiple NPs induced a significantly larger reduction in membrane projection area (Figure 4C), suggesting a greater extent of membrane disruption. To highlight the importance of inter-particle interactions in driving the membrane wrinkling, we performed the simulation again with two Janus NPs and increased the inter-particle distance such that the NPs do not experience hydrophobic attraction between one other. As shown in Figure S15, the Janus NPs behave similarly to single Janus NPs. The NP placed above the Ld phase preferentially interacts with the Ld domain, whereas the NP close to the Lo domain fails to disrupt the Lo domain. This result strongly supports that multiple Janus NPs cooperatively deform the lipid membrane. Interestingly, the extent of membrane projection area reduction does not seem to scale proportionally with the number of Janus NPs, as the total membrane projection area decreased \sim 15% in the presence of four Janus NPs and \sim 7.5% for single Janus NP. It is plausible that when multiple Janus NPs aggregated due to the inter-particle hydrophobic attraction, their hydrophobic hemispheres are only partially available to extract lipids from membranes. Nevertheless, their collective interactions caused a more predominant local deformation of the membrane (Figure 4A at 1.00 μ s) than that by a single Janus NP.

Next, we asked: what is the composition of lipids extracted by Janus NPs? Are the extracted lipids of the same composition as that of the Ld domain? To answer this question, we counted the number of lipids, including DOPC, DPPC, and Chol molecules that were within 0.6 nm proximity from the Janus NPs to obtain the total number of lipids that absorbed to the particles (referred to as "in-contact lipids" for simplicity). We then calculated the percentages of each lipid with respect to the in-contact lipids. We performed the calculation for four different membrane compositions: 2:2:1 (DOPC:DPPC:Chol), 1:1:1, 1:3:1, and 1:2:2 (Figure \$16). Each of the four compositions mimics what was used experimentally, which represents a broad area of the two-phase coexistence region in the DOPC:DPPC:Chol phase diagram.³⁰ Similar to the 2:2:1 bilayer, the 1:2:2 bilayer suffered from a wrinkling induced by multiple Janus NPs (Figure S17; Videos S9 and \$10). For each of the four membrane compositions examined, we plotted the composition of in-contact lipids at 0, 0.10, 0.30, 0.50, 0.70, 0.90, and 1.00 μs, in a ternary plot (Figure 4D). For all four membrane compositions, the composition of in-contact lipids not only was different from the initial composition of Ld domains (detailed compositions are in Table S1), but also changed with simulation time. If we assume that the in-contact lipids largely represent lipids that are extracted by Janus NPs, the data indicates that more DPPC and Chol are extracted as the Janus NP-membrane interaction progress. This suggests that, while the Janus NPs predominantly extract DOPC from the Ld domain at the beginning of interaction, they could extract lipids from both Ld and Lo phases at later time points (Figure S18). This is also demonstrated by the



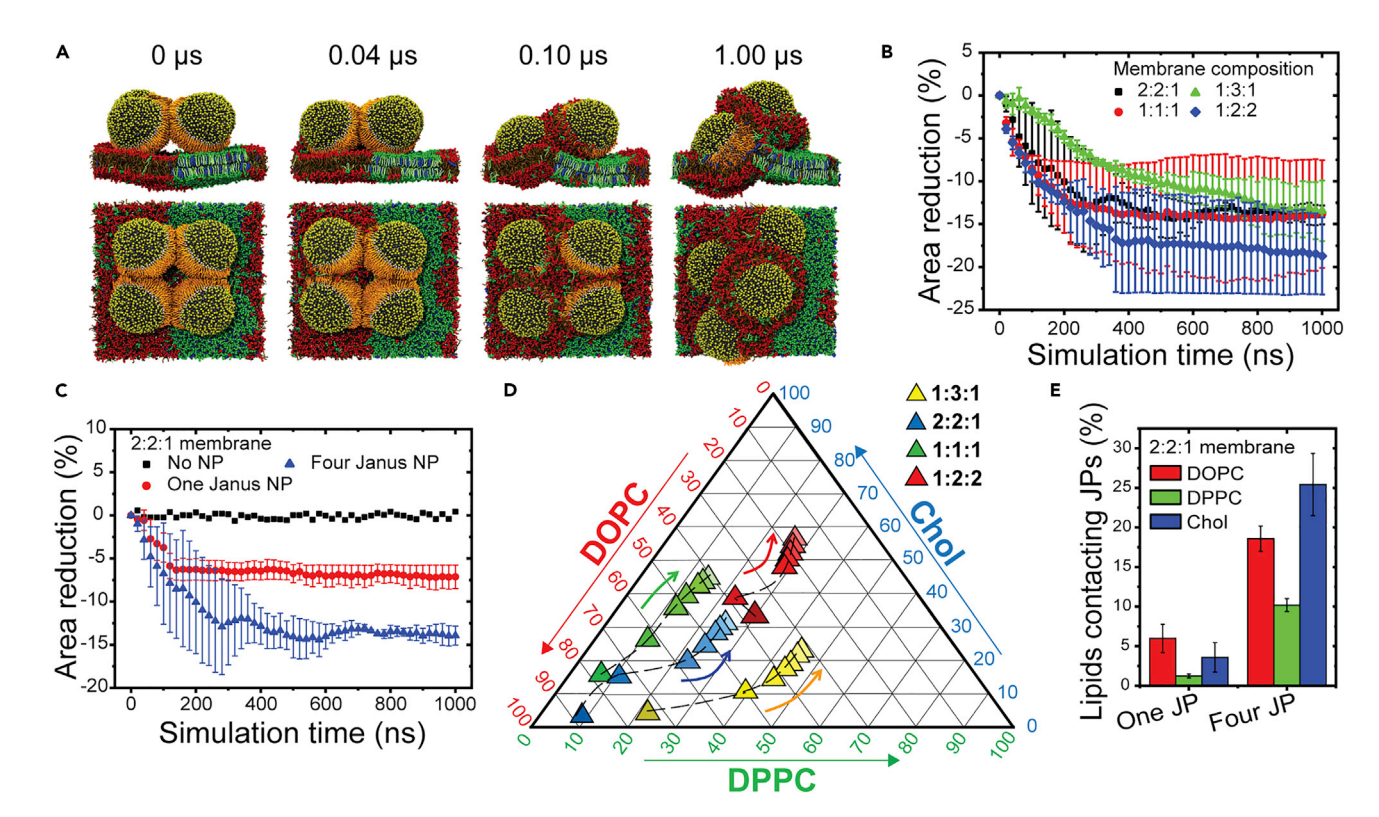


Figure 4. Coarse-grained MD simulations of multiple Janus NPs interacting with planar lipid membranes

(A) Coarse-grained MD simulation of four Janus NPs (core diameter $D_{NP} = 10$ nm) inserting into and wrinkling a phase-separated membrane composed of 2:2:1 DOPC:DPPC:Chol.

(B) Comparison of the total projected area of membranes of various lipid compositions in the presence of four Janus NPs. Data are represented as mean \pm SEM from three independent samples.

(C) Comparison of the total projected area of a lipid bilayer as a function of time in the presence of a single Janus NP versus four Janus NPs. Data are represented as mean \pm SEM from three independent samples.

(D) A ternary plot showing changes in the composition of lipids in contact with Janus NPs as a function of simulation time (within $1.00 \mu s$) for membranes of different lipid compositions. Arrows indicate changes in compositions of in-contact lipids as a function of time: 0, 0.10, 0.30, 0.50, 0.70, 0.90, and 1.00 μs evolvement from the beginning of the simulation to the end. Data are represented as mean from three independent samples.

(E) Comparison of percentage of lipids in contact with Janus NPs in the presence of single and four Janus NPs. Dimension of all lipid membranes is $\sim 30 \times 30 \text{ nm}^2$. Data are represented as mean \pm SEM from three independent samples. See also Figures S14–S18; Tables S1 and S2; Videos S7, S8, S9, and S10.

difference in the area reduction of the Lo domain for all four membranes at the early stage (t = $0.10 \, \mu s$) and at the end of the MD simulation (t = $1.00 \, \mu s$) (Figure S13). Interestingly, we found that lipids in contact with multiple Janus NPs have a higher content of DPPC and Chol than the lipids in contact with a single Janus NP (Figure 4E). One possible explanation is that in Janus NPs aggregates their hydrophobic hemispheres are oriented toward one another. This creates a hydrophobic space that is favorable for DPPC and Chol lipids after the extraction of DOPC lipids. Additionally, we found in the simulation that the adsorption of multiple Janus NPs can hinder lipid diffusion (Table S2), which can potentially facilitate the extraction of the DPPC and Chol lipids from the membrane.

Our simulation results from the planar membrane models together quantitatively confirm the experimental observations that Janus NPs preferentially bind to Ld domains and extract lipids in a domain-selective and time-dependent mechanism. The selective binding of Janus NPs to Ld domains, combined with lipid extraction, plausibly causes the area shrinking, or even disappearance, of Ld domains in GUVs (Figure 2).

Janus nanoparticles compress the vesicle membrane

We have previously shown that lipid extraction by Janus NPs can cause a compression effect on single-component vesicles. ²⁵ Do Janus NPs induce a similar compression effect on the phase-separated vesicles? If so, how are the morphologies of Ld and Lo domains impacted by the compression effect? Experimentally,



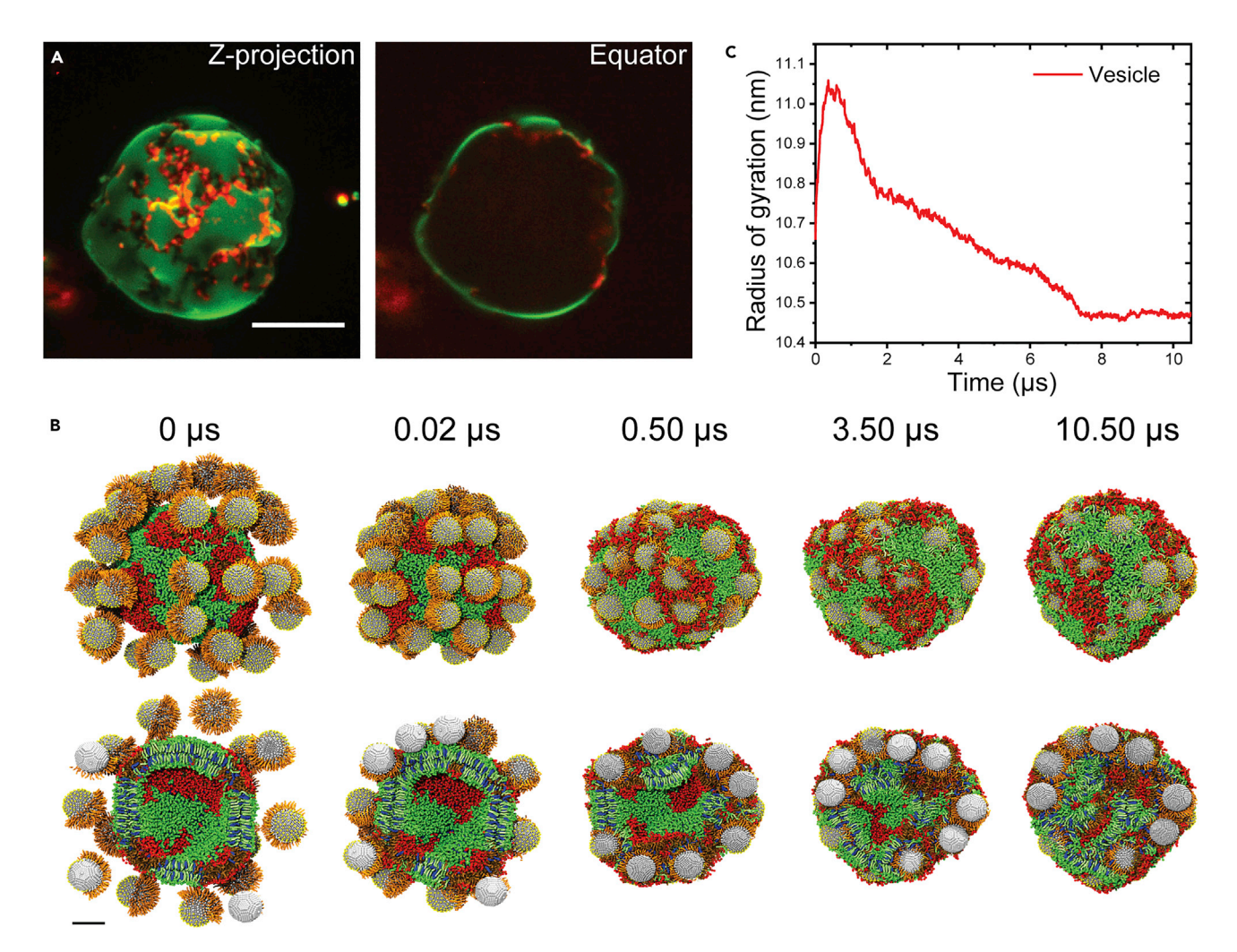


Figure 5. Compression of phase-separated vesicles by Janus NPs

(A) Z-projection (left) and equatorial (right) images of a 1:2:2 vesicle with bulging Lo domains in the presence of Janus NPs. Ld and Lo domains are labeled by RhB-DOPE (shown in red) and BODIPY-Chol (shown in green), respectively. Scale bar: $10 \mu m$.

(B) MD trajectory and cross-sectional snapshots of a 3:4:3 (DUPC:DPPC:Chol) vesicle (diameter = 25 nm) interacting with 38 Janus NPs (core diameter $D_{NP} = 5 \text{ nm}$). The phase-separated vesicle contains Ld domains enriched in DUPC (red beads and brown bonds) and Lo domains enriched in DPPC and Chol (green beads, lime, and blue bonds). Scale bar: 5 nm.

(C) A plot showing the radius of gyration (R_g) of the vesicle in (B) as a function of simulation time (total simulation time 10.5 μ s). See also Figures S19–S21 and Video S11.

we observed that for a fraction of the GUVs, especially those of the 1:2:2 (DOPC: DPPC: Chol) composition, the shrinking and disappearance of Ld domains induced by Janus NPs eventually led to the deformation of the entire GUV membrane that mostly had Lo domains remaining (Figure 5A and more images in Figure S19). The Janus NPs, which were wrapped with lipids mostly from the Ld domains, formed long chain-like aggregations that spanned across the entire GUV membrane in areas where the membrane bulged. These observations suggest a collective compression generated by the Janus NPs. We investigated this phenomenon further using MD simulations. Instead of using a planar membrane with a finite size limit ($\sim 30 \times 30 \text{ nm}^2$), we performed MD simulation on a phase-separated vesicle model. For this model, the vesicle diameter was chosen to be 25 nm to balance the accuracy and the efficiency of computation as mentioned earlier. As shown in Figure S20, the model of a 25 nm-diameter vesicle exhibiting microdomain phase formation was obtainable after reasonable computational time, but doing this on an even larger scale would be too time-consuming to acquire a phase-separated vesicle. Moreover, the solvent-free MARTINI force field was adapted to exclude water molecules to reduce significantly the computational cost as we only look into the interaction between Janus NPs and the vesicle.





reports on DOPC:DPPC:Chol microdomain separation using dry MARTINI force field, we replaced DOPC with 1,2-dilinoleoyl-sn-glycero-3-phosphocholine (DUPC), a double unsaturated lipid which has been used in simulations with phase-separated vesicles. 46 Many studies have adopted this polyunsaturated lipid instead of DOPC to reproduce the experimentally observed phase separation of DOPC:DPPC:Chol membranes. 36,41,47 Consequently, we reduced the size of Janus NP from 10 nm to 5 nm, so that we can observe in simulation both lipid extraction by Janus NPs and NP aggregation on the vesicle surface. The lipid composition used for the vesicle model was 3:4:3 (DUPC:DPPC:Chol), because this ratio facilitates obvious domain formation in vesicle structure with reasonable computational cost.

To obtain a well phase-separated 25 nm-diameter vesicle, a production run was performed at least 10 μs (Figure S20). After the phase-separated vesicle was fully equilibrated, we added 38 Janus NPs (core diameter $D_{NP} = 5$ nm) randomly near the vesicle (Figure 5B at 0 μ s) and then performed an over-10- μ s MD simulation to allow for sufficient NP-membrane interaction. We found that Janus NPs quickly interacted with the vesicle within 0.02 µs and favorably disrupted the Ld domains (red beads and brown bonds) after 0.50 µs (Video S11). By calculating the vesicle radius in simulation using gmx gyrate, 48 we found that the vesicle continuously shrank during interaction with Janus NPs and stabilized after 8.00 µs (Figure 5C). The reduction in vesicle size agrees with the experimental observation and indicates the collective compression effect of Janus NPs on the vesicle membrane. Since our experimental data suggest that the vesicle compression is due to a combination of lipid extraction and attraction between Janus NPs, we sought to test this hypothetical model in simulation. To verify the experimental observation that Janus NPs aggregated over time, we calculated the inter-particle radial distribution function (RDF) profile (Figure S21A). In the beginning, there was no evident peak in the RDF curve indicating no particle aggregation. When the simulation progressed to $0.50 \,\mu s$, the particle started to aggregate, leading to an emerging peak in RDF (orange curve). At $t = 3.50 \mu s$ (green curve), the amplitude of the peak reached maximum, indicating the strongest aggregation of the particles. There was a similar trajectory of the RDF of the DOPC lipids extracted by the particles by the time of 3.50 μs (Figure S21B). The DOPC lipids were initially away from the Janus NPs (red curve), but were in proximity with the NPs at $0.50 \, \mu s$, and then formed complexes with the Janus NPs at $3.50 \, \mu s$ (green curve). The degree of lipid extraction remained consistent with the highest RDF peak until the end of the simulation. Overall, our simulation results suggest that the Janus NP-induced vesicle deformation is a result of two factors: lipid extraction and inter-particle attraction. The lipid extraction is driven by hydrophobic attraction between the Janus NPs and lipids. The inter-particle attraction leads to the formation of the chain-like aggregation of Janus NPs on membranes, as we observed experimentally. Therefore, a high local density of Janus NPs is necessary to generate a stronger cooperative compression effect on the vesicle's membrane.

Conclusion

In this study, we investigated the interaction of amphiphilic Janus NPs, which are hydrophobic on one hemisphere and cationic on the other, with multi-component GUVs exhibiting phase-separated lipid microdomains. We integrated advanced fluorescence microscopy experiments with coarse-grained MD simulations to quantify Janus NP-membrane interactions, including binding kinetics of Janus NPs to different membrane domains and membrane compression induced by Janus NPs. Our results reveal that Janus NPs induce a rich spectrum of membrane transformations in multi-component phase-separated vesicles, many of which were not observed in single-component vesicles in our previous studies.²⁵ Specifically, we made a few key findings. (1) Janus NPs preferentially bind to the DOPC-rich Ld domains in GUV membranes and disrupt mostly the Ld domains by extracting lipids onto their hydrophobic hemispheres. Using MD simulations, we identified not only the exact compositions of lipids in contact with the Janus NPs, but also how the extracted lipid compositions change with time. Such dynamic evolvement of Janus NP-lipid interactions was unknown before. (2) Janus NPs, which were partially wrapped by lipids, form chain-like aggregates on GUV membranes, dragging the Ld domains with them to re-organize. This is driven largely by the inter-particle hydrophobic interactions, further confirmed by coarse-grained MD simulations. (3) Lipid extraction by multiple Janus NPs on the same GUV leads to the shrinking and even disappearance of the Ld membrane domains, which effectively alters the overall membrane composition of the GUVs. The Janus NPs concurrently generate a global compression force on the DPPC-rich Lo domains that remain in the vesicle's membrane, causing those domains to bulge. Based on these findings, we conclude that the selective binding of amphiphilic Janus NPs to the Ld membrane domains leads to domain-selective disruption and compression of lipid vesicles.

Preferential association of NPs with specific membrane domains is known to depend on the surface chemistry of NPs⁴⁹ and the mechanical properties of the membrane domains.⁵⁰ Previous atomistic simulations



have shown that amphiphilic Janus NPs preferentially insert into Ld membrane domains that have less stringent packing constraints compared to Lo domains. ¹⁸ In contrast, our study reveals Janus NP-membrane interactions on a significantly larger length scale by examining the collective membrane compression effect of multiple Janus NPs on micron-sized vesicle membranes. Our findings here highlight the importance of understanding NP-induced membrane compression on cell plasma membranes, by detailing how such compressive effects manifest on a phase-separated membrane. These fundamental understandings pave the way toward utilizing the unique surface anisotropy of Janus NPs to tailor their interactions with different biological membranes.

Limitations of the study

The experiments in this study were done using 100 nm NPs, but the MD simulations were performed using 10 nm NPs due to limitations of computational resources and time. In light of these complications, we reduced the size of the simulation system including the gold core of Janus NPs and the GUV membrane. Nevertheless, the computational models in this work are mainly used to identify interactions that drive the NP-induced membrane disruption; they are not meant to reproduce the exact experimental conditions.

STAR*METHODS

Detailed methods are provided in the online version of this paper and include the following:

- KEY RESOURCES TABLE
- RESOURCE AVAILABILITY
 - O Lead contact
 - Materials availability
 - O Data and code availability
- METHOD DETAILS
 - O Janus NP fabrication and characterization
 - O GUV electroformation and imaging
 - O Janus NP-membrane binding energy
 - MARTINI force field descriptions
 - O Planar membrane model
 - O Janus NP-planar membrane simulations
 - O Potential mean force simulations
 - O Vesicle model construction with dry MARTINI
 - MD analysis
- QUANTIFICATION AND STATISTICAL ANALYSIS

SUPPLEMENTAL INFORMATION

Supplemental information can be found online at https://doi.org/10.1016/j.isci.2022.105525.

ACKNOWLEDGMENTS

We thank Dr. Jim Powers at the IUB Light Microscopy Imaging Center and Dr. Giovanni Gonzalez-Gutierrez at IUB Physical Biochemistry Instrumentation Facility for assistance with instrument use. Fabrication and characterization of Janus NPs were done at the IUB Nanoscale Characterization Facility. This work was supported by the National Science Foundation under Grant No. 1705384 to Y.Y. and No. 1755779 to Y. L.

AUTHOR CONTRIBUTIONS

J. T. W., D. N., Y. L, and Y. Y. designed research. J.W. performed experiments and analyzed experimental data. D. N. performed simulations and analyzed simulation data. J. T. W., D. N., Y. L, and Y. Y. wrote the article

DECLARATION OF INTERESTS

The authors declare no competing interests.

INCLUSION AND DIVERSITY

We support inclusive, diverse, and equitable conduct of research.



Received: July 27, 2022 Revised: October 12, 2022 Accepted: November 4, 2022 Published: December 22, 2022

REFERENCES

- Walther, A., and Müller, A.H.E. (2013). Janus particles: synthesis, self-assembly, physical properties, and applications. Chem. Rev. 113, 5194–5261.
- 2. Jiang, S., Chen, Q., Tripathy, M., Luijten, E., Schweizer, K.S., and Granick, S. (2010). Janus particle synthesis and assembly. Adv. Mater. 22, 1060–1071.
- 3. Yi, Y., Sanchez, L., Gao, Y., and Yu, Y. (2016). Janus particles for biological imaging and sensing. Analyst 141, 3526–3539.
- Agrawal, G., and Agrawal, R. (2019). Janus nanoparticles: recent advances in their interfacial and biomedical applications. ACS Appl. Nano Mater. 2, 1738–1757.
- Le, T.C., Zhai, J., Chiu, W.-H., Tran, P.A., and Tran, N. (2019). Janus particles: recent advances in the biomedical applications. Int. J. Nanomedicine 14, 6749–6777.
- 6. Wu, L.Y., Ross, B.M., Hong, S., and Lee, L.P. (2010). Bioinspired nanocorals with decoupled cellular targeting and sensing functionality. Small 6, 503–507.
- Lee, S., Zhang, Z., and Yu, Y. (2021). Real-time simultaneous imaging of acidification and proteolysis in single phagosomes using bifunctional Janus-particle probes. Angew. Chem. Int. Ed. Engl. 60, 26734–26739.
- 8. Leroueil, P.R., Berry, S.A., Duthie, K., Han, G., Rotello, V.M., McNerny, D.Q., Baker, J.R., Jr., Orr, B.G., and Holl, M.M.B. (2008). Wide varieties of cationic nanoparticles induce defects in supported lipid bilayers. Nano Lett. 8, 420–424.
- Li, S., and Malmstadt, N. (2013). Deformation and poration of lipid bilayer membranes by cationic nanoparticles. Soft Matter 9, 4969–4976.
- Lee, H., and Larson, R.G. (2008). Lipid bilayer curvature and pore formation induced by charged linear polymers and dendrimers: the effect of molecular shape. J. Phys. Chem. B 112, 12279–12285.
- Lee, H., and Larson, R.G. (2006). Molecular dynamics simulations of PAMAM dendrimerinduced pore formation in DPPC bilayers with a coarse-grained model. J. Phys. Chem. B 110, 18204–18211.
- Jing, B., and Zhu, Y. (2011). Disruption of supported lipid bilayers by semihydrophobic nanoparticles. J. Am. Chem. Soc. 133, 10983– 10989.
- Pogodin, S., Werner, M., Sommer, J.-U., and Baulin, V.A. (2012). Nanoparticle-induced permeability of lipid membranes. ACS Nano 6, 10555–10561.

- 14. Van Lehn, R.C., Atukorale, P.U., Carney, R.P., Yang, Y.-S., Stellacci, F., Irvine, D.J., and Alexander-Katz, A. (2013). Effect of particle diameter and surface composition on the spontaneous fusion of monolayer-protected gold nanoparticles with lipid bilayers. Nano Lett. 13, 4060–4067.
- Shen, Z., Ye, H., Yi, X., and Li, Y. (2019). Membrane wrapping efficiency of elastic nanoparticles during endocytosis: size and shape matter. ACS Nano 13, 215–228.
- Li, Y., Kröger, M., and Liu, W.K. (2015). Shape effect in cellular uptake of PEGylated nanoparticles: comparison between sphere, rod, cube and disk. Nanoscale 7, 16631– 16646.
- Ding, H.-m., and Ma, Y.-q. (2012). Interactions between Janus particles and membranes. Nanoscale 4, 1116–1122.
- Ou, L., Corradi, V., Tieleman, D.P., and Liang, Q. (2020). Atomistic simulations on interactions between amphiphilic Janus nanoparticles and lipid bilayers: effects of lipid ordering and leaflet asymmetry. J. Phys. Chem. B 124, 4466–4475.
- Lin, X., and Lin, X. (2021). Designing amphiphilic Janus nanoparticles with tunable lipid raft affinity via molecular dynamics simulation. Biomater. Sci. 9, 8249–8258.
- Alexeev, A., Uspal, W.E., and Balazs, A.C. (2008). Harnessing Janus nanoparticles to create controllable pores in membranes. ACS Nano 2, 1117–1122.
- Arai, N., Yasuoka, K., and Zeng, X.C. (2013). A vesicle cell under collision with a Janus or homogeneous nanoparticle: translocation dynamics and late-stage morphology. Nanoscale 5, 9089–9100.
- Lee, K., and Yu, Y. (2019). Lipid bilayer disruption induced by amphiphilic Janus nanoparticles: the non-monotonic effect of charged lipids. Soft Matter 15, 2373–2380.
- 23. Lee, K., Zhang, L., Yi, Y., Wang, X., and Yu, Y. (2018). Rupture of lipid membranes induced by amphiphilic Janus nanoparticles. ACS Nano 12, 3646–3657.
- 24. Lee, K., and Yu, Y. (2018). Lipid bilayer disruption by amphiphilic Janus nanoparticles: the role of Janus balance. Langmuir 34, 12387–12393.
- Wiemann, J.T., Shen, Z., Ye, H., Li, Y., and Yu, Y. (2020). Membrane poration, wrinkling, and compression: deformations of lipid vesicles induced by amphiphilic Janus nanoparticles. Nanoscale 12, 20326–20336.
- 26. Linklater, D.P., Baulin, V.A., Le Guével, X., Fleury, J.-B., Hanssen, E., Nguyen, T.H.P.,

- Juodkazis, S., Bryant, G., Crawford, R.J., Stoodley, P., and Ivanova, E.P. (2020). Antibacterial action of nanoparticles by lethal stretching of bacterial cell membranes. Adv. Mater. 32, 2005679.
- Zhukova, L.V. (2015). Evidence for compression of Escherichia coli K12 cells under the effect of TiO2 nanoparticles. ACS Appl. Mater. Interfaces 7, 27197–27205.
- Ghysels, A., Krämer, A., Venable, R.M., Teague, W.E., Lyman, E., Gawrisch, K., and Pastor, R.W. (2019). Permeability of membranes in the liquid ordered and liquid disordered phases. Nat. Commun. 10, 5616.
- Angelova, M.I., and Dimitrov, D.S. (1986). Liposome electroformation. Faraday Discuss. Chem. Soc. 81, 303–311.
- Veatch, S.L., and Keller, S.L. (2003).
 Separation of liquid phases in giant vesicles of ternary mixtures of phospholipids and cholesterol. Biophys. J. 85, 3074–3083.
- 31. Baumgart, T., Hunt, G., Farkas, E.R., Webb, W.W., and Feigenson, G.W. (2007). Fluorescence probe partitioning between Lo/Ld phases in lipid membranes. Biochim. Biophys. Acta 1768, 2182–2194.
- Ariola, F.S., Li, Z., Cornejo, C., Bittman, R., and Heikal, A.A. (2009). Membrane fluidity and lipid order in ternary giant unilamellar vesicles using a new bodipy-cholesterol derivative. Biophys. J. 96, 2696–2708.
- 33. Kaizuka, Y., and Groves, J.T. (2004). Structure and dynamics of supported intermembrane Junctions. Biophys. J. 86, 905–912.
- Wei, L., Zhao, X., Chen, B., Li, H., Xiao, L., and Yeung, E.S. (2013). Frozen translational and rotational motion of human immunodeficiency virus transacting activator of transcription peptide-modified nanocargo on neutral lipid bilayer. Anal. Chem. 85, 5169–5175.
- Gumí-Audenis, B., Costa, L., Ferrer-Tasies, L., Ratera, I., Ventosa, N., Sanz, F., and Giannotti, M.I. (2018). Pulling lipid tubes from supported bilayers unveils the underlying substrate contribution to the membrane mechanics. Nanoscale 10, 14763–14770.
- Canepa, E., Salassi, S., de Marco, A.L., Lambruschini, C., Odino, D., Bochicchio, D., Canepa, F., Canale, C., Dante, S., Brescia, R., et al. (2020). Amphiphilic gold nanoparticles perturb phase separation in multidomain lipid membranes. Nanoscale 12, 19746– 19759.
- Stottrup, B.L., Veatch, S.L., and Keller, S.L. (2004). Nonequilibrium behavior in supported lipid membranes containing cholesterol. Biophys. J. 86, 2942–2950.

iScience

Article



- Seu, K.J., Pandey, A.P., Haque, F., Proctor, E.A., Ribbe, A.E., and Hovis, J.S. (2007). Effect of surface treatment on diffusion and domain formation in supported lipid bilayers. Biophys. J. 92, 2445–2450.
- Sarić, A., and Cacciuto, A. (2012). Fluid membranes can drive linear aggregation of adsorbed spherical nanoparticles. Phys. Rev. Lett. 108, 118101.
- Carpenter, T.S., López, C.A., Neale, C., Montour, C., Ingólfsson, H.I., Di Natale, F., Lightstone, F.C., and Gnanakaran, S. (2018). Capturing phase behavior of ternary lipid mixtures with a refined martini coarsegrained force field. J. Chem. Theory Comput. 14, 6050–6062.
- Pantelopulos, G.A., Nagai, T., Bandara, A., Panahi, A., and Straub, J.E. (2017). Critical size dependence of domain formation observed in coarse-grained simulations of bilayers composed of ternary lipid mixtures. J. Chem. Phys. 147, 095101.
- 42. Yu, Y., Vroman, J.A., Bae, S.C., and Granick, S. (2010). Vesicle budding induced by a pore-forming peptide. J. Am. Chem. Soc. *132*, 195–201.
- Schäfer, L.V., de Jong, D.H., Holt, A., Rzepiela, A.J., de Vries, A.H., Poolman, B., Killian, J.A., and Marrink, S.J. (2011). Lipid packing drives the segregation of transmembrane helices into disordered lipid domains in model membranes. Proc. Natl. Acad. Sci. USA 108, 1343–1348.
- Lemkul, J.A., and Bevan, D.R. (2010).
 Assessing the stability of Alzheimer's amyloid protofibrils using molecular dynamics.
 J. Phys. Chem. B 114, 1652–1660.

- Arnarez, C., Uusitalo, J.J., Masman, M.F., Ingólfsson, H.I., de Jong, D.H., Melo, M.N., Periole, X., de Vries, A.H., and Marrink, S.J. (2015). Dry Martini, a coarse-grained force field for lipid membrane simulations with implicit solvent. J. Chem. Theory Comput. 11, 260–275.
- Marrink, S.-J. Martini Tutorials: Lipids. http:// www.cgmartini.nl/index.php/tutorials/37tutorial2/312-tutorial-lipids.
- Risselada, H.J., and Marrink, S.J. (2008). The molecular face of lipid rafts in model membranes. Proc. Natl. Acad. Sci. USA 105, 17367–17372.
- Marchetto, A., Si Chaib, Z., Rossi, C.A., Ribeiro, R., Pantano, S., Rossetti, G., and Giorgetti, A. (2020). CGMD platform: integrated web servers for the preparation, running, and analysis of Coarse-grained molecular dynamics simulations. Molecules 25. E5934.
- Chen, X., Tieleman, D.P., and Liang, Q. (2018). Modulating interactions between ligand-coated nanoparticles and phase-separated lipid bilayers by varying the ligand density and the surface charge. Nanoscale 10, 2481–2491.
- Chaudhury, A., Varshney, G.K., Debnath, K., Das, G., Jana, N.R., and Basu, J.K. (2021). Compressibility of multicomponent, charged model biomembranes tunes permeation of cationic nanoparticles. Langmuir 37, 3550–3562
- Marrink, S.J., Risselada, H.J., Yefimov, S., Tieleman, D.P., and de Vries, A.H. (2007). The MARTINI force field: coarse grained model for biomolecular simulations. J. Phys. Chem. B 111, 7812–7824.

- Wassenaar, T.A., Ingólfsson, H.I., Böckmann, R.A., Tieleman, D.P., and Marrink, S.J. (2015). Computational lipidomics with insane: a versatile tool for generating custom membranes for molecular simulations.
 J. Chem. Theory Comput. 11, 2144–2155.
- Jo, S., Kim, T., Iyer, V.G., and Im, W. (2008). CHARMM-GUI: a web-based graphical user interface for CHARMM. J. Comput. Chem. 29, 1859–1865.
- Castillo, N., Monticelli, L., Barnoud, J., and Tieleman, D.P. (2013). Free energy of WALP23 dimer association in DMPC, DPPC, and DOPC bilayers. Chem. Phys. Lipids 169, 95–105.
- Humphrey, W., Dalke, A., and Schulten, K. (1996). VMD: Visual molecular dynamics. J. Mol. Graph. 14, 33–38. 27-8.
- Lindahl, E., Abraham, M.J., Hess, B., and van der Spoel, D., GROMACS 2020 (2020). Manual.
- 57. Lee, J., Cheng, X., Swails, J.M., Yeom, M.S., Eastman, P.K., Lemkul, J.A., Wei, S., Buckner, J., Jeong, J.C., Qi, Y., et al. (2016). CHARMM-GUI input generator for NAMD, GROMACS, AMBER, OpenMM, and CHARMM/OpenMM simulations using the CHARMM36 additive force field. J. Chem. Theory Comput. 12, 405–413.
- Brooks, B.R., Brooks, C.L., Iii, Mackerell, A.D., Jr., Nilsson, L., Petrella, R.J., Roux, B., Won, Y., Archontis, G., Bartels, C., Boresch, S., et al. (2009). CHARMM: the biomolecular simulation program. J. Comput. Chem. 30, 1545–1614.
- Alex, H.d.V. (2017). Do-order tools. http:// www.cgmartini.nl/images/tools/do-ordergmx5.py.





STAR*METHODS

KEY RESOURCES TABLE

REAGENT or RESOURCE	SOURCE	IDENTIFIER
Chemicals, peptides, and recombinant proteins		
Aminated silica nanoparticles (100 nm in diameter)	NanoComposix (San Diego, CA, USA)	cat# SIAN100-25M
Chromium pellets (99.99% purity)	Kurt J. Lesker, Co. (Jefferson Hills, PA, USA)	cat# EVMCR35D
Gold pellets (99.99% purity)	Kurt J. Lesker, Co. (Jefferson Hills, PA, USA)	cat# EVMAUXX40G
Cy5 N-hydroxysuccinimide ester	Lumiprobe Corporation (Hunt Valley, MD, USA)	cat# 23020
Octadecane-1-thiol	Sigma-Aldrich (St. Louis, MO, USA)	cat# O1868-25ML
HEPES powder	Sigma-Aldrich (St. Louis, MO, USA)	cat# H3375-100G
Cholesterol	Sigma-Aldrich (St. Louis, MO, USA)	cat# C8667-1G
1,2-dioleoyl-sn-glycero-3-phosphocholine (DOPC)	Avanti Polar Lipids, Inc. (Alabaster, AL, USA)	cat# 850375C-500mg
1,2-dipalmityl-sn-glycero-3-phosphocholine (DPPC)	Avanti Polar Lipids, Inc. (Alabaster, AL, USA)	cat# 850355C-200mg
1,2-dioleoyl- <i>sn</i> -glycero-3-phosphoethanolamine- N-(lissamine rhodamine B sulfonyl) (RhB-DOPE)	Avanti Polar Lipids, Inc. (Alabaster, AL, USA)	cat# 810150C-5mg
23-(dipyrrometheneboron difluoride)-24- norcholesterol (BODIPY-Chol)	Avanti Polar Lipids, Inc. (Alabaster, AL, USA)	cat# 810255P-1mg
Deposited data		
Fluorescence microscopy images	This paper	Figshare: https://doi.org/10.6084/ m9.figshare.21277800.v1
Software and algorithms		
lmageJ	National Institutes of Health	https://imagej.nih.gov/ij/
GROMACS 2020	GNU Library General Public License v2.1 or later	https://zenodo.org/record/ 3562495#.YzyTa3bMLIU
Standard MARTINI force field	Marrink, S. J. et al. ⁵¹	http://cgmartini.nl/index.php/downloads
Modified MARTINI force field	Carpenter, T. S. et al. ⁴⁰	https://pubs.acs.org/doi/abs/ 10.1021/acs.jctc.8b00496
Standard dry MARTINI force field	Arnarez, C. et al. ⁴⁵	http://md.chem.rug.nl/index.php/ force-field-parameters/dry-martini
INSANE (INSert membraNE)	Wassenaar, T. A. et al. ⁵²	http://www.cgmartini.nl/index.php/downloads/tools/239-insane
Weighted Histogram Analysis Method	Lemkul, J. A. et al. ⁴⁴	https://manual.gromacs.org/ documentation/5.1/onlinehelp/gmx-wham
CHARMM-GUI	Jo, S. et al. ⁵³	https://www.charmm-gui.org/
Membrane ordering	Castillo, N. et al. ⁵⁴	https://www.dsimb.inserm.fr/ ~luca/downloads/
Visual Molecular Dynamics	Humphrey, W. et al. ⁵⁵	https://www.ks.uiuc.edu/Development/ Download/download.cgi?PackageName=VMD

(Continued on next page)





Continued		
REAGENT or RESOURCE	SOURCE	IDENTIFIER
Other		
Indium tin oxide-coated slides	Delta Technologies, Ltd. (Loveland, CO, USA)	Cat# CG-90IN-X204

RESOURCE AVAILABILITY

Lead contact

Further information and requests for resources and reagents should be directed to and will be fulfilled by the lead contact, Yan Yu (yy33@indiana.edu).

Materials availability

This study did not generate new unique reagents.

Data and code availability

Fluorescence microscopy images have been deposited to figshare and are publicly available as of the date of publication. DOI is listed in the key resources table. This paper does not report original code. Any additional information required to reanalyze the data reported in this paper is available from the lead contact upon reasonable request.

METHOD DETAILS

Janus NP fabrication and characterization

Microscope slides were first cleaned with piranha solution (75:25 v:v concentrated H₂SO₄:30% H₂O₂) and subsequently rinsed with ultrapure water. Aminated silica NPs (100 nm in diameter) were drop cast onto clean microscope slides to form a sub-monolayer of particles. An Edwards thermal evaporation system (Nanoscale Characterization Facility at Indiana University) was used to sequentially deposit a thin coating of chromium (5 nm) followed by a gold coating (25 nm) onto one hemisphere of the NPs. To make the gold cap on Janus NPs hydrophobic, particle monolayers were immediately immersed in 2 mM 1-octadecanethiol in ethanol for at least 12 h, and then sonicated off of microscope slides before use. Janus NPs were spun down using differential centrifugation (4 times at 100 \times g, 4 times at 500 \times g) to remove large particle aggregates. For experiments with fluorescently labeled particles, freshly sonicated Janus NPs were mixed with Cy5 in 2 mM HEPES (pH 7.4) for 1 h. Final concentrations during the dye conjugation reaction were ca. 5 pM Janus NPs and 1.5 μ M Cy5. After labeling, particles were washed with ethanol at least ten times to remove free dyes. Immediately before mixing with GUVs, particles were washed with 100 mM glucose aqueous solution at least three times to remove ethanol and match the osmolarity of the external GUV medium. Janus NPs were characterized using scanning electron microscopy (Nanoscale Characterization Facility at Indiana University). Hydrodynamic radius and zeta potential of particles were characterized using a Malvern Zetasizer (Nanoscale Characterization Facility at Indiana University). Particle concentration was measured using Particle Metrix ZetaView (Nanoscale Characterization Facility at Indiana University).

GUV electroformation and imaging

DOPC, DPPC, and cholesterol were mixed in desired molar ratios (2:2:1, 1:1:1, 1:3:1, and 1:2:2) in chloroform to prepare stock solutions. In each mixture, BODIPY-Chol (0.2 mol%) and RhB-DOPE (0.2 mol%) were included to fluorescently label Lo and Ld phases, respectively. Approximately 10 μ L of lipid stock solution (5.0 mg/mL) was spread onto an ITO-coated glass slide to make a lipid film. Residual chloroform was removed by drying lipids under nitrogen for 30 min. The dried lipid film was hydrated with 100 mM aqueous sucrose solution, and the lipid coated ITO slide was immediately assembled with another ITO slide and a silicone spacer (1.7 mm thick) into an electroformation chamber. GUVs were electroformed at 60°C for 2 h under a sinusoidal AC field (3.4 V_{rms} , 5 Hz) and used within 2 h after electroformation. Glass coverslips for fluorescence microscopy imaging of GUVs were cleaned by sonication in 70% ethanol. For experiments in the presence of NPs, Janus NPs (suspended in 100 mM glucose) were mixed 2:1 (v:v) with GUVs in 100 mM sucrose for a final particle concentration of 40 pM, and the mixture was directly added to the imaging chamber. Experiments without Janus NPs used a 2:1 (v:v)





mixture of GUVs in 100 mM sucrose and 100 mM glucose. This sucrose-glucose mixture helps GUVs to settle to the coverslip surface. Epi fluorescence images were acquired using a Nikon Eclipse Ti-E inverted microscope with either a $40 \times /0.95$ NA Nikon air objective or a $100 \times /1.49$ NA Nikon TIRF oil-immersion objective. Confocal images were acquired using an Olympus OSR Spinning Disk Confocal microscope (Light Microscopy Imaging Center at Indiana University) with a $100 \times /1.35$ NA Olympus silicone-immersion objective. All images were processed using ImageJ. For vesicle miscibility experiments, a Bioptechs FCS2 temperature-controlled stage insert with a thermocouple to monitor sample temperature was used. The sample temperature was increased from $30^{\circ}\text{C}-45^{\circ}\text{C}$ in intervals of 5°C . At each interval, images were acquired after temperature had equilibrated for at least 5 min. A $40 \times /0.95$ NA Nikon air objective was used in temperature-controlled experiments to prevent heat loss from objective-sample contact.

Janus NP-membrane binding energy

GUVs (2:2:1 DOPC:DPPC:Chol) were electroformed in 500 mM aqueous sucrose solution. After electroformation, vesicles were kept at room temperature for 30 min to allow Ld-Lo phase separation. GUVs were then ruptured on piranha-etched glass coverslips by mixing Sorenson's phosphate buffer (100 mM, pH 7.4) and GUV solution at a 2:1 (v:v) ratio.³³ After 30 min, the bilayers were washed 15 times with 100 mM aqueous glucose solution to remove unruptured GUVs. The phase-separated bilayer was imaged using epi-fluorescence microscopy first. Cy5-labeled Janus NPs (15 pM) were then added to the bilayer and imaged using total internal reflectance fluorescent (TIRF) microscopy on a Nikon Eclipse Ti microscope equipped with a 100x/1.49 NA TIRF objective lens. At the end of TIRF imaging, the phase-separated bilayer was imaged again using epi fluorescence microscopy.

To measure single particle-membrane kinetics, epi-fluorescence images before and after particle addition were used to generate masks of membrane domains using ImageJ. Briefly, RhB-DOPE fluorescence from epi-fluorescence was used to set a threshold to make a mask of the Ld domains. Because BODIPY-Chol partitions into both Ld and Lo domains, the Lo mask was generated by subtracting the Ld mask from the BODIPY-Chol mask. Each mask was applied to the NP fluorescence channel to isolate particles bound to the Lo domains from those bound to Ld domains. Bound particles were manually counted for each time point in the resulted domain-specific image series. The single-particle binding rate constant was calculated using the following equation:³⁴

$$\frac{dN}{dt} = -k_a C_S C_{JP}$$

where dN/dt is the rate of particle binding per unit area, k_a is the second order binding rate constant, C_s is the number of binding sites per unit area on the lipid membrane, and C_{JP} is the bulk Janus NP concentration. C_s was estimated by calculating the number of particles which could fit into $1 \, \mu m^2$ assuming hexagonal packing. To calculate the binding energy (E_a) of Janus NPs to different membrane domains, the Arrhenius equation was employed:

$$E_A = [\ln(Q) - \ln(k_a)]k_bT$$

Where Q is a diffusion collisional constant, k_b is the Boltzmann constant, and T is the absolute temperature. Q for the system is 9.285 \times 10¹¹ M⁻¹ s⁻¹ for 100 nm Janus NPs assuming the JP-membrane association is limited by the diffusion of particles.²³

MARTINI force field descriptions

Coarse-grained MD simulations were implemented using GROMACS (2020 version).⁵⁶ Atoms were represented by coarse-grained (CG) beads using the MARTINI force field.⁵¹ In this force field, each bead represents up to four heavy atoms and is characterized as one of four types: polar, nonpolar, apolar, or charged, which correspond to the labels of P, N, C, and Q, respectively. Bead types used for each lipid in this research are shown in Figure 3A. For phase-separated planar membranes, a modified version from standard MARTINI was adapted to ensure the formations of Ld and Lo domains in the bilayer model. Two lipid species used in the planar bilayer models were dipalmitoylphosphatidylcholine (DPPC) and single-unsaturated dioleoylphosphatidylcholine (DOPC). For the vesicle's membrane, a standard dry MARTINI force field was used.⁴⁵ To ensure the generation of a phase-separated vesicle model, 1,2-dilino-leoyl-sn-glycero-3-phosphocholine (DUPC) was used instead of DOPC.



Planar membrane model

All initial bilayer models were constructed using the INSANE (INSert membraNE) script.⁵² This tool provides a convenient way to adjust the size and composition of a MARTINI bilayer model. The membranes were constructed from DOPC, DPPC and Chol. Four different lipid compositions were investigated in this study: 2:2:1 (DOPC:DPPC:Chol), 1:3:1, 1:1:1 and 1:2:2. Each system contained about 3,700 CG lipids of all species combined and 256,000 CG waters. The total system size was about 30 \times 30 \times 35 nm³ to make sure it can handle four Janus NPs of 10 nm in core diameter. Each planar membrane system was initiated with energy minimization using the steepest descent method (5000 steps), followed by a successive isothermal-isobaric (NPT) equilibration simulation with the number of particles (N), constant pressure (P), and temperature (T) all kept constant. The NPT simulation was performed for 30 ns (timestep = 30 fs) and then followed by a 15 μ s phase-separated production simulation (timestep = 30 fs). Reaction-field electrostatics was used with a Coulomb cutoff of 1.1 nm and dielectric constants of 15 or 0 within or beyond this cutoff distance, respectively. Lennard-Jones interactions were cut off at 1.1 nm, where the potential energy was shifted to zero. Constant temperature was maintained at 298 K via separate coupling of the solvent (water) and membrane (DOPC, DPPC and Chol) components to v-rescaling thermostat (relaxation time = 1.0 ps). Pressure was semi-isotropically coupled at 1.0 bar. Berendsen scheme was used for the NPT equilibration (relaxation time = 12.0 ps and compressibility = $3 \times 10^{-4} \text{ bar}^{-1}$). After equilibration, Parrinello-Rahman barostat was used for the production run.

Janus NP-planar membrane simulations

The Janus NP model used in our simulation was adapted from our recent work. 25 Briefly, the gold (Au) core of the Janus NP was cut out of a bulk FCC lattice with a constant of 0.408 nm. The size of the Au core was 10 nm, which was selected based on a trade-off between computational efficiency and accuracy. The Au core was constructed with inert metal beads C5 and two distinctly surrounding bead types on its surface. On the hydrophilic hemisphere of the core, its surface was surrounded with hydrophilic positive charged Qd bead with an areal density of 2.5 nm^{-2} . On the hydrophobic part of the core, its surface was covered with sulfur beads (No) with an area density of 4.7 nm^{-2} . Each No bead is bonded with a hydrophobic alkyl chain represented by four C1 beads to mimic the octadecane carbon chain. The Au-Au interactions in the core were treated with harmonic bond potentials using a force constant of $10,000 \text{ kJ mol}^{-1}$ to ensure their rigidity. The Au-Qd and Au-N₀ interactions were applied with a force constant of $6,400 \text{ kJ mol}^{-1}$ with an equilibrium bond length of 0.24 nm. A harmonic bond potential force constant of $1,250 \text{ kJ mol}^{-1}$ with an equilibrium bond length of 0.47 nm and a cosine angle potential of 180° with a force constant of 25 kJ mol⁻¹ were applied to the bonds in the ligand. For lipid bilayer model, DOPC consisted of headgroup (Qa, Q0 and Na) and tails (C1 and C4) beads, DPPC with headgroup (Qa, Q0 and Na) and lime tail (C1) beads, Chol was constituted with SP1 beads.

The dynamics of single and multiple Janus NPs was subjected to a series of MD simulation steps. Initially, a single Janus NP was positioned close to the Ld-Lo boundary with a center-of-mass (COM) distance of 9.5 nm above the middle plane of the bilayer. In the case of multiple Janus NPs, four particles were placed above the membrane with close distances to each other to accelerate the cooperative effect of multiple NPs. Subsequently, a steepest descent minimization with 10,000 steps was performed to resolve steric clashes. This step was followed by a 20-ns equilibration using an NPT ensemble. The production run was then performed for each system for 1.00 µs. The timestep of all Janus NP-membrane interaction simulations was set at 20 fs. The reaction-field electrostatics was used with a Coulomb cutoff of 1.4 nm and dielectric constants of 15 or 0 within or beyond this cutoff distance, respectively. For non-bonded interactions, Lennard-Jones force field were cut off at 1.4 nm, where the potential energy was shifted to zero. Constant temperature was maintained at 298 K via separate coupling of the solvent (water), membrane (DOPC, DPPC and Chol) and Janus NP components to v-rescaling thermostats (relaxation time = 1.0 ps). In both equilibration and production stages, pressure was semi-isotropically coupled at 1.0 bar and controlled by Berendsen barostat (relaxation times = $12.0 \, \text{ps}$ and compressibility = $3 \times 10^{-4} \, \text{bar}^{-1}$). For each NP-membrane model, we ran three independent simulations and then calculated the mean and standard deviation values for statistical comparisons.

Potential mean force simulations

The potential of mean force (PMF) profile was achieved by means of the umbrella sampling technique ⁴⁴ to investigate the binding energy of Janus NP to different lipid domains. We chose two membranes for the PMF measurements: pure Ld membrane (contained only DOPC) and pure Lo membrane (contained only





DPPC and Chol). The Ld membrane model contained 1568 CG molecules of DOPC, and the Lo membrane model contained 940 CG molecules of DPPC and 625 CG molecules of Chol. Each lipid bilayer was equilibrated for 1.00 μ s to ensure the membrane equilibrium prior to being further used. The simulations were performed by pulling the Janus NP towards the membrane in the z-direction. The reaction coordinate (variable) was specified as the distance between the center-of-mass (COM) of the particle and the center of the membrane. Umbrella harmonic potential was applied using a force constant of 1000 kJ mol⁻¹ nm⁻². Windows of 0.2 nm width were used to sample the distance in the range 5–10 nm with a simulated time of 20 ns/100 ns for the equilibration/production run for each window, respectively. After the simulations, PMF profiles were extracted using the Weighted Histogram Analysis Method (WHAM), which was included in GROMACS as the wham utility. ⁴⁴ Binding energy was determined as the difference between the highest and lowest values in the PMF curve.

Vesicle model construction with dry MARTINI

Dry MARTINI force field was adapted to explore the interactions between Janus NPs and a lipid vesicle. The dry MARTINI is a solvent-free force field. ⁴⁵ There has been no modified version of the dry MARTINI force field to guarantee a water-exclusive multidomain formation for the DOPC:DPPC:Chol vesicle. Strikingly, it has been shown that a phase-separated vesicle could be generated with the standard dry MARTINI force field using a composition of DPPC, Chol and a double-unsaturated phosphocholine, namely 1,2-dilinoleoyl-sn-glycero-3-phosphocholine (DUPC). ⁴⁶ Within the MARTINI force field approach, the doubly unsaturated beads in DUPC can induce stronger repulsion towards DPPC when compared to DOPC (single-unsaturated lipid). As a driving force, it can accelerate the phase separation in the bilayer as well. Therefore, DOPC is replaced with DUPC in this solvent-free vesicle simulation.

A DUPC:DPPC:Chol vesicle of 25 nm in diameter was simulated following the standard procedure presented by CHARMM-GUI. 53,57,58 The vesicle was initially generated using a vesicle maker tool in CHARMM-GUI with a specific ratio of input lipids. Here, the ratio of DUPC: DPPC: Chol was selected as 3:4:3 and the total numbers of DUPC, DPPC, and Chol in the vesicle membrane were 1658, 2210 and 1658 respectively. The vesicle was equilibrated by energy-minimization (steepest descent, 10 000 steps) followed by subsequent NPT simulations using increasing time steps from 2.0 fs to 20 fs. The vesicle modeling used second-order stochastic dynamics (SD) integrator in GROMACS that is efficiently used for solvent-free system. 45,46 For equilibrium, temperature of the system was set at 298 K using v-rescaling thermostat (relaxation time = 1.0 ps) and pressure was set at 1.0 bar using Berendsen isotropic pressure controller (relaxation time = 5.0 ps and compressibility = $4.5 \times 10^{-5} \text{ bar}^{-1}$). For production run, temperature was set at 298 K (relaxation time = 0.1 ps) without pressure coupling. The production run should be over 10 μ s (time step = 30 fs) to obtain a phase-separated vesicle as shown in Figure S20. After generating the phase-separated vesicle, the system was randomly mixed with 38 Janus NPs (core diameter $D_{NP} = 5$ nm). Afterwards, the system model was implemented with an energy minimization (steepest descent, 10 000 steps), an NPT equilibration (time step = 20 fs), and a long production run over 10 µs (time step = 30 fs) to observe the evolution of the lipid vesicle interacting with multiple Janus NPs. The equilibration was set at 298 K and 1.0 bar using v-rescaling thermostat (relaxation time = 1.0 ps) and Berendsen controller (relaxation time = 5.0 ps and compressibility = $4.5 \times 10^{-5} \text{ bar}^{-1}$), respectively. The production run was set at 298 K (relaxation time = 0.1 ps) without pressure coupling.

MD analysis

The number of lipids contacting Janus NPs, referred to as *in-contact* lipids, was evaluated using the *gmx mindist* with a cut-off distance of 0.6 nm. The density of lipids in the bilayer was calculated using *gmx densmap*. To quantify vesicle's shrinkage, the radius of gyration of the vesicle was monitored with the *gmx gyrate* module. The radial distribution function (RDF) is a histogram of the calculated distances between a selected atom/group to a reference atom/group. Here the RDF of the Janus NPs corresponding to themselves can be used to quantify the particle aggregate, while the RDF of the DUPC molecules toward the particle (reference) indicates the attraction of DUPC lipids to the particles. The RDF was calculated using *gmx rdf* with the bin size of 0.1 nm. The averaged order parameters of the lipid tails in the membrane were calculated using a custom Python script (*do-ordered-gmx5.py*) available elsewhere. Specifically, the lipid order parameters were defined as $S_{CC} = 0.5 \times (3\cos^2\theta - 1)$, where θ is the angle between the bond formed by two coarse-grained beads and the bilayer normal. The landscape of order



parameters over the lipid bilayer was obtained using an MD analysis tool developed by N. Castillo et al. 54 Snapshots during the simulation were rendered by the Visual Molecular Dynamics (VMD) software. 55

QUANTIFICATION AND STATISTICAL ANALYSIS

Statistical details are provided in the figure captions. Unless noted, error bars represent standard error of the mean (SEM).